Journal of Catalysis **211,** 265–272 (2002)
doi:10.1006/jcat.2002.3725

Energetics of Potassium Loss from Styrene Catalyst Model Components: Reassignment of K Storage and Release Phases

Andrzej Kotarba,[1] Irmina Kruk, and Zbigniew Sojka

Faculty of Chemistry, Jagiellonian University, Ingardena 3, 30-060 Cracow, Poland

Received April 29, 2002; revised June 13, 2002; accepted June 13, 2002

Thermal desorption of potassium ions and atoms from K-doped iron oxides (Fe_3O_4, Fe_2O_3) and potassium ferrites ($KFeO_2$, $K_2Fe_{22}O_{34}$) that are the principal phases of the iron oxide catalysts for dehydrogenetion of ethylbenzene to styrene was investigated. From the Arrhenius plots the activation energies for desorption of K and K^+ were determined in the process temperature range for each of the phases. Based on these results the desorption energies obtained previously for the commercial styrene catalysts were reinterpreted and the K storage and release phases were explicitly identified. The results were discussed in terms of a surface stability diagram. It was shown that in the active state of the catalyst the $K_2Fe_{22}O_{34}$ component is responsible for excessive potassium release. The proposed optimal morphology of the catalyst grain consists of a core $K_2Fe_{22}O_{34}$ surrounded by a compact shell of active $KFeO_2$, while a core and cracked-shell model was adapted to account for the potassium desorption data from the real catalysts.

Key Words: **alkali promoter; potassium desorption; styrene catalysts; $KFeO_2$; $K_2Fe_{22}O_{34}$; Fe_3O_4; Fe_2O_3.**

1. INTRODUCTION

Dehydrogenation of ethylbenzene (EB) to styrene belongs to one of the most important industrial processes used to produce valuable commodities such as polystyrene, acrylonitrile-butadiene-styrene (ABS), and styrene-butadiene latex. The current worldwide production of styrene monomer reaches the level of 20×10^6 ton/year (1) and most of it is made over the iron oxide catalyst (2). Promotion with potassium can increase the activity of the catalyst by an order of magnitude (3, 4). Although this process was developed in the 1930s, since then research has continued to improve the catalyst formulation, process route, and the reactor design as well (1, 5–11).

Because of the thermodynamic limitation, formation of styrene is favored by low partial pressure of EB and hydrogen. Thus, to provide the heat for reaction and prevent overreduction and coking of the catalyst, the dehydrogenation process is usually carried out in the presence of overheated steam at ambient or lower pressure and at temperature as high as 823–973 K (12). Such severe conditions give rise to gradual deterioration of the catalyst performance shortening its lifetime to 1–2 years. Taking into account the large scale of styrene production, this significantly increases the process operational costs.

The scrutiny of the open literature reveals three main reasons for the iron oxide catalyst deactivation: (i) formation of carbonaceous deposition, (ii) change in oxidation state of iron, and (iii) loss of potassium promoter (13). It has been shown that all three reasons are mutually related. The deposition of coke is accompanied by excessive reduction of iron and the carbide mechanism was developed to account for the chemistry of this process (14). Although the role of coke is still controversial it is generally accepted that its presence is harmful for the catalyst performance. Historically, addition of potassium to iron oxide catalysts was believed to assist in coke removal through its gasification with the co-fed steam. However, recent work has shown that the interaction of potassium with the iron oxide matrix is much more complex than a mere catalyst of coke gasification (*vide infra*).

The detailed solid-state chemistry of the iron oxide catalyst and the nature of active phases under real process conditions have been extensively studied. In a series of meticulous papers, Muhler, Schlögl, and co-workers advanced a complete life cycle of the catalyst (15–20). They showed a comprehensive role of potassium in the solid-state and surface chemistry of the catalyst transformation, from the precursor oxide, through active ferrite, to the deactivated oxide states. The initial and final states of the iron oxide catalyst correspond to K-doped hematite and magnetite with segregated KOH, respectively. In the course of the solid-state restructuring two ferrite phases, $KFeO_2$ and $K_2Fe_{22}O_{34}$, appear. The active state of the catalyst is assigned to the equilibrium between them. Once the active state is established, two different deactivation processes develop along with a reversible one, which due to the deposition of coke on the catalyst surface, in addition to a slow irreversible deactivation pathway, which is due to the loss of

[1] To whom correspondence should be addressed. E-mail: kotarba@chemia.uj.edu.pl.

0021-9517/02 $35.00

potassium promoter from the catalyst surface and its migration along the bed. The chemical form in which potassium migrates is KOH, which is produced by the reduction of the active ferrites into the waste Fe_3O_4. Recently a concise review of those processes was published (21).

Obviously, the simplest remedy for ubiquitous loss of potassium is overcharging, and indeed the industrial loadings may reach even the level of 30 wt% (7). An alternative solution could be an enhancement of the potassium surface stability by chemical means. The latter method, however, requires a better understanding of the potassium-loss mechanism including the determination of the promoter stability energetics and identification of K storage and release phases involved in the catalyst lifecycle.

Surface science investigations on well-defined model iron oxide films prepared by the deposition of metallic potassium on Fe_3O_4 (111) followed by annealing to 970 K revealed clearly the presence of $KFeO_2$ and $K_2Fe_{22}O_{34}$ ferrite in the catalyst active state but the stability of potassium in these phases was not explicitly verified. It was presumed that the $K_2Fe_{22}O_{34}$ acts as a K storage, while the potassium-rich $KFeO_2$ phase, produced on top of $K_2Fe_{22}O_{34}$, is responsible for the catalyst activity. The treatment with water vapor, even at very low partial pressures, leads to potassium depletion in the near-surface region and results in catalyst deactivation. At the final state of the evolution separated phases of Fe_3O_4 and KOH were observed.

Desorption of potassium from the real styrene catalysts was studied by Holmlid *et al*. (22–25), and was recently summarized (26). The ultrahigh vacuum molecular-beam techniques were employed to study the characteristics of potassium desorption from several commercial fresh and spent catalysts. The results were epitomized in the form of an energy diagram (23). The large differences in K desorption energies measured for both catalysts reflect their solid-state restructuring over prolonged time onstream. Taking into account the catalyst deactivation mechanism (15, 19), the observed K desorption energies of 1.0, 1.7, and 3.1 eV were tentatively assigned to the presumed K_2O, $KFeO_2$, and $K_2Fe_{22}O_{34}$ components, respectively. This assignment, however, is not univocal since the desorption experiments were performed on industrial catalysts and the invoked phases were actually not identified.

The aim of the current work was to elucidate the energetics of potassium desorption from four single key phases involved in the iron oxide catalyst evolution (Fe_3O_4, Fe_2O_3, $KFeO_2$, $K_2Fe_{22}O_{34}$), to identify explicitly the potassium storage and release phases, and to determine the potassium-loss channels (atomic and ionic). The species resolved thermal alkali desorption (SR-TAD) method was used to follow the fluxes of desorbing K and K^+ and their temperature dependence. This method previously was successfully used to study the stability of potassium promoter on other iron catalysts (27–32).

2. EXPERIMENTALS AND METHODS

2.1. Materials

The model systems, i.e., two iron oxides promoted with potassium (K/Fe_2O_3 and K/Fe_3O_4) and two ferrites ($K_2Fe_{22}O_{34}$, $KFeO_2$) were prepared. All reactants used in the synthesis were of analytical-grade quality. Commercial α-Fe_2O_3 (Merck) was used as a starting material for the synthesis. The Fe_3O_4 spinel was obtained at 1370 K by passing a CO_2/CO mixture (20 : 1) over the parent hematite placed in a platinium boat for 24 h. The K/Fe_2O_3 and K/Fe_3O_4 samples with the potassium loading of 10–50 ppm were obtained by dry impregnation with 1–5 μL of 1 M KOH aqueous solution.

Potassium ferrites can be prepared by calcining a suitable proportion of hematite with KNO_3 or K_2CO_3 in the temperature range 1070–1470 K (33–36). A calculated phase diagram published elsewhere (20) provides useful guidelines for the corresponding substrate ratio and temperature of the particular synthesis. The $KFeO_2$ (33) and $K_2Fe_{22}O_{34}$ (35, 36) ferrites were prepared by reaction of stoichiometric amounts of K_2CO_3 with α-Fe_2O_3 according to the procedure given elsewhere. The mixtures of finely ground powders placed in a porcelain crucible were heated at the rate of 7.5 K/min in air until the final temperatures of 1070 K for $KFeO_2$ and 1470 K for $K_2Fe_{22}O_{34}$ was reached. In the latter case the heating was halted at 1170 K and after cooling down to room temperature the mixture was reground for 15 min and heated again at 1470 K for 5 h.

Since both ferrites are quite sensitive to humidity (37) they were kept in a desiccator and investigated immediately after the synthesis. Changes in the ferrite structures detectable by XRD were observed after one day exposure to air. However, in the case of the samples preserved in a desiccator over dry KOH, no such changes were detected even after several months indicating that the bulk integrity was maintained. The XPS investigations in C 1s regions revealed that the possible contamination by carbonates is rather small, since the C 1s shoulder at about 289 eV assigned to carbonate barely emerged above the tail of adventitious carbon. Accordingly, the associated carbonate oxygen shoulder, though its intensity is expected to be considerably greater ($I_O(CO_3) \sim 3\sigma_O/\sigma_C I_C(CO_3) \sim 10$), was also weak. Thus, we may reasonably assume that the contamination by carbonate was rather small.

2.2. Techniques

The phase identity was verified by X-ray diffraction. The measurements were performed with Cu$K\alpha$ radiation (40 kV, 30 mA, and Ni filter) in the Bragg–Brentano geometry using PW 3020 and X'pert Pro Philips powder diffractometers.

The specific surface area of the samples was determined in a flow mode by means of N_2 adsorption. The measurements were performed using a Quantasorb apparatus according to the BET method.

The morphology of the samples was examined with a Philips scanning electron microscope model XL 30 using 1,500 and 10,000 magnifications.

The surface composition was studied with an ESCA 100 spectrometer (VSW Scientific Instruments) using Mg$K\alpha$ radiation (1253.6 eV, 120 W). The samples were prepared by deposition from hexane suspension. A hemispherical electrostatic analyzer with 100-mm diameter and 22- or 44-eV pass energy was used. The background pressure during the experiments was greater than 10^{-8} mbar. The spectra were collected at 0.06-eV steps and accumulated using 4–20 scans to improve the signal-to-noise ratio. The binding energies of the surface components were determined by referencing the adventitious carbon C 1s line (BE = 284.6 eV). The accuracy of the binding-energy determination was estimated to be ±0.1 eV.

The SR-TAD experiments were carried out in a vacuum apparatus with a background pressure of 10^{-7} mbar. The samples were heated from room temperature to 950 K with a Boralectric heater (Tectra GmbH) in intermittent mode at the rate of 5 K/min. The desorbing fluxes of potassium atoms and ions were followed. The atomic flux of K was determined by means of a surface ionization detector (28) with the rhenium filament heated to 1500 K. Due to low ionization potential of potassium, only K atoms were surface-ionized at such conditions; the efficiency was close to 100% (38). Potassium ions were measured simply by the ion collector in a field ionization detector (27) with both electrodes grounded. The K^+ ions formed at the surface were accelerated toward the detector by an electric potential of +60 V applied to the sample. In all measurements, the resultant positive current was measured directly with a digital electrometer Keithley 6512. For the thermal desorption experiments the samples were pressed to form wafers of 10-mm diameter and typical mass of 100 mg.

3. RESULTS AND DISCUSSION

3.1. Catalyst Characterization

The phase identity of the synthesized ferrites was confirmed by XRD measurements based on the JCPDS-ICDD and ICSD databases as references (Figs. 1 and 2). The diffraction patterns were indexed within *Pbca* ($KFeO_2$) and $P6_3/mmc$ ($K_2Fe_{22}O_{34}$) space groups. The analysis revealed that the synthesized ferrites were virtually monophasic.

Scanning electron micrographs showed that the morphologies of Fe_3O_4 and $KFeO_2$ resemble that of the parent α-Fe_2O_3. Generally, the 8-μm sized aggregates composed of smaller 3–4-μm crystallites predominated the picture.

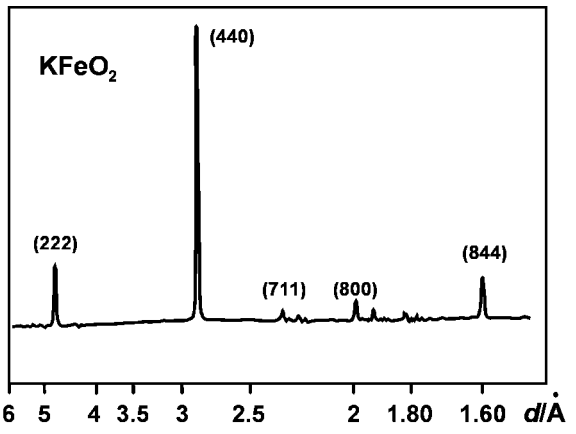

FIG. 1. X-ray diffraction patterns of $KFeO_2$ indexed within *Pbca* space group.

They were loosely intermixed with scarce groupings consisting of 2–3 particles. The crystallites were interconnected through necks giving rise to a coarse structure. The extent of aggregation slightly increased when passing from Fe_2O_3 to Fe_3O_4 and was significantly higher for $KFeO_2$. In the case of $K_2Fe_{22}O_{34}$ the shape of crystallites was distinctly different and resembled that of a single crystal of K^+-β-ferrite with ideal stoichiometric composition (35). The well-developed crystallites forming hexagonal plates of 0.8-μm diameter and thickness of 0.2 μm were observed in the pictures.

The SEM observations were corroborated by surface-area measurements. For all investigated samples the surface areas were of the same order and ranged from 4 m^2/g for the most sintered $K_2Fe_{22}O_{34}$ to 17 m^2/g for $KFeO_2$. The collation of the particle size and the BET surface area results are given in Table 1. In the case of Fe_3O_4 and $KFeO_2$ the surface areas doubled upon the synthesis. Since the average size of the crystallites remained practically the same as in the parent hematite, during this process the enduring porosity of these samples was apparently enhanced. In contrast, for

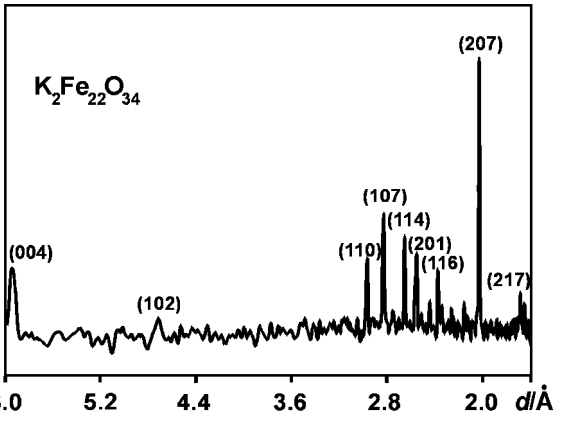

FIG. 2. X-ray diffraction patterns of $K_2Fe_{22}O_{34}$ indexed within $P6_3/mmc$ space group.

TABLE 1

Morphological Characterization of Investigated Samples

Sample	BET surface area ($m^2\ g^{-1}$)	Crystallite average size (μm)	K surface coverage (atoms nm^{-2})
K/Fe_2O_3	6 ± 1	3 ± 1	1.0 ± 0.2
K/Fe_3O_4	13 ± 1	4 ± 1	2.0 ± 0.1
$KFeO_2$	17 ± 1	3 ± 1	9.0 ± 0.1
$K_2Fe_{22}O_3$	4 ± 1	0.8 ± 0.2	2.0 ± 0.2

the $K_2Fe_{22}O_{34}$ ferrite, both the surface area and the crystallite size decreased, indicating that during the synthesis this sample was considerably sintered as one might expect when taking into account the highest temperature (1470 K) of the synthesis.

Potassium surface coverage for K/Fe_2O_3 and K/Fe_3O_4 was calculated from the measured surface area and the loading. In the case of the $K_2Fe_{22}O_{34}$ and $KFeO_2$ ferrites the corresponding surface concentration was assessed from the structure of the (0001) and (001) planes, respectively. The coverage (1–2 atom nm^{-2}) for Fe_2O_3 and Fe_3O_4 was adjusted to the value obtained for $K_2Fe_{22}O_{34}$ because excessive potassium loadings, comparable to the surface concentration in $KFeO_2$, led to the *in situ* formation of surface ferrites during the thermal desorption experiments. As a result the observed desorption energies, which were continuously changed toward the values characteristic of $KFeO_2$ with the increasing K doping, were not diagnostic of the K desorption from iron oxides.

The XPS survey scans indicated that, neglecting the adventitious carbon, only the constituent elements of the investigated oxides were found within the surface layer. The detailed spectra of Fe 2p, K 2p, and O 1s regions allowed determination of the corresponding binding energies. They are summarized in Table 2 and compared with the reference data. The observed binding energies for Fe_2O_3 and Fe_3O_4 remain in good agreement with the published values. In both cases the most diagnostic Fe $2p_{3/2}$ region was dominated by the signal at ~711 eV, which is characteristic of Fe^{3+} ions in octahedral and tetrahedral positions because these coordinations cannot be distinguished by XPS (39–41). The large width of the Fe $2p_{3/2}$ line and the presence of a core-level shake-up satellite at 720 eV are consistent with a high spin configuration of the iron typical O^{2-} environment. The O 1s peak was broad (fwhm = 3.6–3.1 eV) with a shoulder about 1.2 eV above the principal line at 529.5 ± 0.1 eV. The same features in the oxygen core band were observed previously and assigned to the presence of hydroxyl groups on iron oxides (19).

TABLE 2

K 2p, Fe 2p, and O 1s XPS Binding Energies (eV)

Sample	K $2p_{3/2}$	Fe $2p_{3/2}$	O 1s	Ref.
Fe_3O_4	—	710.7	530.0	this work
	—	710.9–711.1	529.8–530.3	[a]
	—	710.8 plane (111)	529.8 plane (111)	(20)
α-Fe_2O_3	—	710.6	529.5	this work
	—	710.5–711.0	529.5–530.0	[a]
	—	711.1 plane (0001)	529.8 plane (0001)	(20)
$KFeO_2$	292.3	709.3	529.4	this work
	292.7	710.2	529.4	(20)
$K_2Fe_{22}O_{34}$	292.3	710.3	529.6	this work
	293.0	710.8	529.8	(20)
Model styrene catalysts	293.6	710.6 (activated)	529.9	(19)
	—	711.1[b]	—	(19)

[a] ThermoVG Scientific database: http://www.lasurface.com/Data_base/Neigbour/Aw_voisin.htm.

[b] After treatment at 900 K in air.

The Fe 2p XPS spectrum of $K_2Fe_{22}O_{34}$ was very similar to that observed for the iron oxides and only the position of the $2p_{3/2}$ line was slightly shifted to lower BE value. The greatest differences were observed for $KFeO_2$ spinel, where the batoenergic shift was the highest. Though a similar effect was observed previously (20), it was, however, less pronounced than in our case. The Fe $2p_{3/2}$ band exhibits a complex structure, and except for the 710.7-eV peak attributable to Fe^{3+}, it can be decomposed into another component at 709.3 eV. Such low value may be indicative of the presence of divalent iron, though it is not a constituent of the $KFeO_2$ ferrite. We think that appearance of Fe^{2+} in the sample is probably due to the *in situ* beam reduction. Such phenomenon was observed several times in XPS studies on transition-metal oxides (42) and its origin was discussed elsewhere (41).

The XPS results were basically in line with previous thorough studies on those systems and since the explicit XPS investigations were beyond the scope of this paper a more in-depth analysis of the data was not attempted. More details can be found, e.g., in a careful XPS study on iron oxide model catalyst that specifically includes Fe_2O_3, Fe_3O_4, $KFeO_2$, and $K_2Fe_{22}O_{34}$ phases (20).

3.2. Thermal Desorption of Potassium

Potassium ionic and neutral desorption curves (plotted in Arrhenius coordinates) obtained for all investigated samples are presented in Figs. 3a, 3b, 4a, and 4b. Due to high values of the correlation coefficients, the activation energies for desorption of potassium ions, $E_d(K^+)$, and atoms, $E_d(K)$, can be reliably determined from the linear parts of the corresponding plots. The values of activation energies are listed in Table 3. For desorption of neutral species the energy barriers varied from 0.83 ($K_2Fe_{22}O_{34}$) to 4.96 eV (K/Fe_2O_3). For ionic desorption the energy range was smaller and changed from 2.33 to 4.16 eV for $K_2Fe_{22}O_{34}$ and K/Fe_2O_3, respectively. Surprisingly, despite the fact that potassium ions cannot be incorporated into the cubic close-packed lattice of magnetite or hematite, because of the large ionic radius of K^+ (138 pm) compared to that of O^{2-} (133 pm), the surface stability of adsorbed potassium on

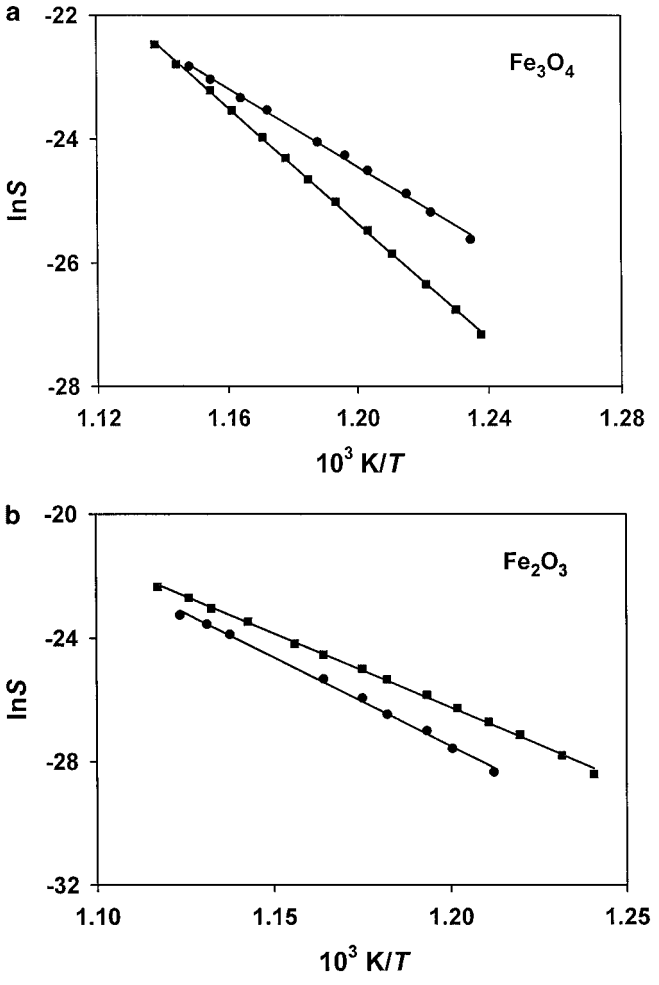

FIG. 3. Arrhenius plots for potassium atoms (●) and ions (■) desorbing from the surface of (a) Fe_3O_4 and (b) Fe_2O_3.

both iron oxides was higher than that chemically bound in the ferrites.

There have been relatively few systematic studies on thermal alkali desorption from oxide surfaces. In all cases reported in the literature, atomic desorption flux dominated in the temperatures up to about 1000 K (43). The same phenomenon was observed for the investigated samples, except for the K/Fe_2O_3, where the ionic flux was slightly higher (Figs. 3 and 4). This is, however, consistent with the measured values of the K and K^+ desorption energies. Indeed, for those samples, where $E_d(K^+) > E_d(K)$ the atomic flux is always favored (23, 25, 30); consequently, for K/Fe_2O_3 with $E_d(K^+) < E_d(K)$, the dominating flux should be the ionic one. This also means that in this case the charge transfer from potassium to hematite was the most effective. Also for this sample, the highest surface stability of potassium was found.

The determined activation energies of desorption can be compared with the results obtained for several commercial styrene catalysts (22–24) and interpreted in terms of the potential energy diagram for interaction of K atoms with the iron oxide surface proposed elsewhere (26). In this model, which epitomizes a good deal of the experimental data, potassium can desorb along covalent or ionic potential energy curves. Since these curves cross along the desorption coordinate several energy pathways are possible, leading to ionic and atomic potassium in different final states (4s, 4p, 3d, etc.) outside the surface.

The activation energies higher than 4 eV observed for K/Fe_2O_3 and K/Fe_3O_4 can be assigned to the desorption

TABLE 3

Activation Energies E_d(eV) for K and K^+ Desorption from K-Doped Iron Oxides and Potassium Ferrites

Sample	$E_d(K)$	$E_d(K^+)$
K/Fe_3O_4	2.73 ± 0.03	4.07 ± 0.02
K/Fe_2O_3	4.96 ± 0.07	4.16 ± 0.02
$KFeO_2$	2.84 ± 0.06	2.95 ± 0.01
$K_2Fe_{22}O_{34}$	0.83 ± 0.01	2.33 ± 0.03

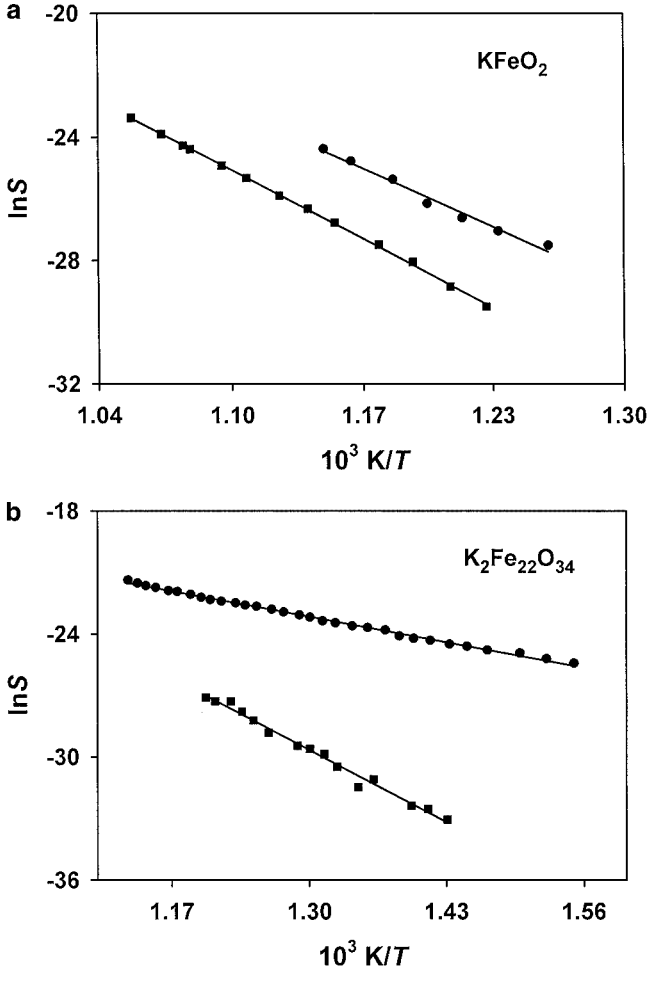

FIG. 4. Arrhenius plots for potassium atoms (●) and ions (■) desorbing from the surface of (a) $KFeO_2$ and (b) $K_2Fe_{22}O_{34}$ ferrites.

process involving the K 3d state. The energies around 3 eV obtained for $KFeO_2$ correlate with potassium desorption to the K 4p state. Since the energy required to reach the 4p state from 4s is equal to 1.6 eV, the desorption energies lower than this correspond to potassium in the final 4s state. Thus the lowest energy of 0.83 eV, which was found for $K_2Fe_{22}O_{34}$, may reasonably be described as the desorption barrier to this state. These crude assignments, based on the empirical approach that was built on the results obtained for commercial styrene catalysts, should be supported by more sophisticated quantum chemical calculations, which are in progress (44).

The value of 0.83 ± 0.01 eV measured for K desorption from $K_2Fe_{22}O_{34}$ was exactly the same as the energy (0.84 ± 0.07 eV) reported for the active commercial styrene catalyst (23, 25). Another characteristic value of potassium desorption from styrene catalyst, which was repeatably observed in Holmlid's investigations, is 3.1 ± 0.2 eV, which again corresponds well with 2.84 ± 0.06 eV and 2.94 ± 0.01 eV observed by us for $KFeO_2$. Taking into account that $K_2Fe_{22}O_{34}$ was considered as the most stable compound in styrene catalyst (3, 4) the authors simply associated the higher desorption energy of 3.1 eV with that phase. Consequently the lower barrier (0.84 ± 0.01 eV) for K emission was assigned to $KFeO_2$, the second ferrite phase postulated in the active catalyst. In contrast to these studies in the current investigation we measured desorption barriers from pure, well-defined phases separately. The energies obtained in our investigations remain in a very good agreement with those reported for real catalysts (23–25), indicating that such phases are indeed present at the catalyst surface. But actually the original attribution should be reversed, because as the lower energy was observed for $K_2Fe_{22}O_{34}$ and the higher energy for $KFeO_2$. Such reassignment was reinforced additionally by the desorption energetics of the ionic flux. Here again the K^+ barrier determined for $KFeO_2$ was distinctly higher than that established for $K_2Fe_{22}O_{34}$.

The desorption results are consistent with the crystallographic structure of both ferrites (20, 35). $K_2Fe_{22}O_{34}$ has the hexagonal layered structure and it can be considered to be built up from spinel blocks of γ-Fe_2O_3 and separated by alkali metal layers. $KFeO_2$ is tetragonal and its lattice is not congruent with that of Fe_2O_3. Since this ferrite has no layer structure, K, Fe, and O constituents are spatially more uniformly distributed. Thus, one may reasonably expect that relatively loose potassium from exposed layers of $K_2Fe_{22}O_{34}$ can be desorbed more easily than the confined potassium in the $KFeO_2$ ferrite.

3.3. Relevance of K Energetics Characteristics for Catalyst Formation and Deterioration

As already mentioned, the life cycle of the styrene catalyst involves the following transformation steps: K-doped

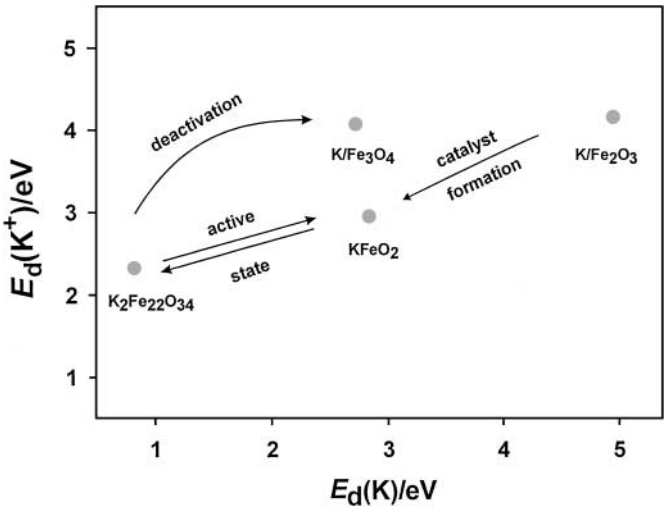

FIG. 5. Desorption energies of potassium ions $E_d(K^+)$ and atoms $E_d(K)$ plotted against each other and their relevance to the deactivation process of the iron oxide catalyst.

$Fe_2O_3 \rightarrow KFeO_2 \leftrightarrow K_2Fe_{22}O_{34} \rightarrow Fe_3O_4$ with segregated KOH. Potassium stability along this pathway is represented by the desorption energies for atoms and ions in Fig. 5. The plot presents a direct link between the potassium desorption parameters, $E_d(K^+)$ and $E_d(K)$, and the function of the particular phases of the iron oxide catalyst in the potassium-loss mechanism. Indeed from the position in the diagram the K storage/release phases can be identified readily.

Even quick inspection of Fig. 5 shows that the catalyst formation entails dramatic decrease in potassium stability when the parent K-doped hematite transforms into ternary compounds. In the active state, conditioned by the equilibrium between the ferrites, the appearance of the $K_2Fe_{22}O_{34}$ phase with the smallest energies of K and K^+ desorption simultaneously opens an efficient channel for potassium loss from the catalyst. Thus, paradoxically, the catalyst activity is unavoidably related to an extensive depletion of the promoter.

Although further evolution of the system leads to an increase in the stability of potassium as Fe_3O_4 is gradually formed, the favorable equilibrium condition of the reactivity breaks down and the catalyst progressively deteriorates due to the segregation of the promoter from the ferrite. Thus, to maintain the active-state equilibrium and to hinder the undesired simultaneous removal of potassium, the grain morphology of the catalyst has to be appropriately engineered from the viewpoint of potassium loss. The catalytically active $KFeO_2$ phase should be exposed, forming an outerlayer, whereas the $K_2Fe_{22}O_{34}$ phase, which serves as a potassium reservoir, is displaced into the catalyst bulk. Such morphology does not only assure the mutual contact between both ferrites but, more importantly, the $KFeO_2$ ferrite of higher potassium stability (potassium sink) envelops the $K_2Fe_{22}O_{34}$ phase acting as the potassium source

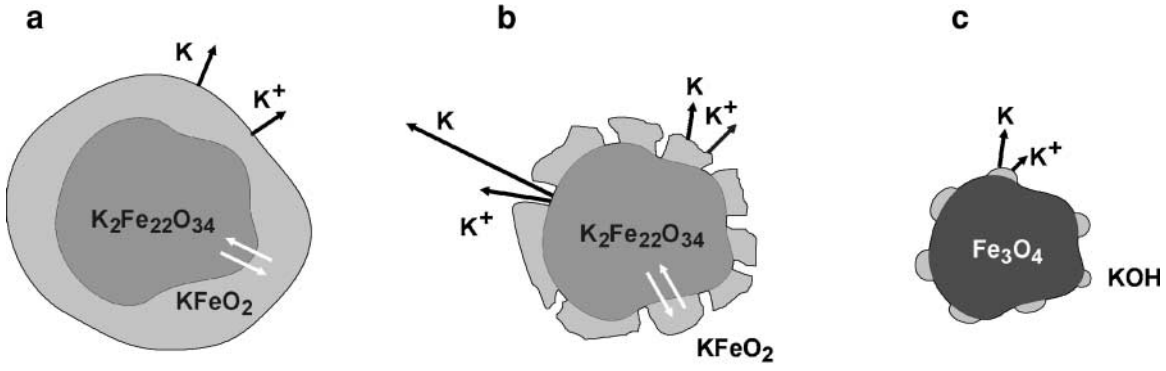

FIG. 6. Schematic representation of (a) an ideal compact core and shell, (b) a more realistic core and cracked shell, and (c) deactivated catalyst grain morphology.

(Fig. 6, diagram a). In this simple way the harmful K loss can be hampered.

Since in the case of the real active catalyst the energies characteristic of K desorption from both ferrites were observed simultaneously, it is indicated that those phases were exposed together. Thus, the proposed idealized core and compact shell morphology of the catalyst (Fig. 6, diagram a) should be replaced by a more realistic core and cracked-shell model (Fig. 6, diagram b). In such case the exposed patches of $K_2Fe_{22}O_{34}$ form the gates for quite efficient potassium depletion because, particularly for this phase, the desorption barriers are the smallest. The function of the $K_2Fe_{22}O_{34}$ ferrite may then change from beneficial to noxious depending on the catalyst morphology. When covered by $KFeO_2$, it acts as the potassium supplier maintaining the active state of the surface, but, when exposed to open space, $K_2Fe_{22}O_{34}$ becomes the potassium waster principally responsible for the excessive loss over prolonged time on stream. The resulting K-impoverished ferrite phases transform into the magnetite decorated with KOH (Fig. 6, diagram c). Although this apparently improves the stability of K, which can be inferred from the stability diagram (Fig. 5), such a state is totally inactive.

4. CONCLUSIONS

The thermal desorption of potassium atoms and ions from model compounds found in the commercial iron oxide catalyst for styrene production allowed the determination of their potassium storage and release properties. The method proved to be useful in the characterization of potassium surface states by the activation energies for K and K^+ desorption. The stability for K atoms varies as $K/Fe_2O_3 \gg KFeO_2 > K/Fe_3O_4 \gg K_2Fe_{22}O_{34}$, while the corresponding series for K^+ is $K/Fe_2O_3 > K/Fe_3O_4 \gg KFeO_2 > K_2Fe_{22}O_{34}$. The results are discussed in terms of a core and cracked-shell model of the iron oxide catalyst with the $K_2Fe_{22}O_{34}$ phase responsible for the potassium loss inside, and the active $KFeO_2$ component responsible for loss outside, the grain.

ACKNOWLEDGMENTS

This work was done within Research Project 3T09A17219, sponsored by the Polish Committee for Scientific Research. The authors thank Prof. Shigeru Ito from the Science University of Tokyo for providing the details of $K_2Fe_{22}O_{34}$ ferrite synthesis and Rafał Molencki for the stylistic improvement.

REFERENCES

1. Addiego, W. P., Liu, W., and Boger, T., *Catal. Today* **69**, 25 (2001).
2. Menon, P. G., and Delmon, B., *in* "Handbook of Heterogeneous Catalysis" (G. Ertl, H. Knözinger, and J. Weitkamp, Eds.), Vol. 1, p. 101. VCH, Weinheim, 1997.
3. Hirano, T., *Appl. Catal.* **26**, 65 (1986).
4. Hirano, T., *Appl. Catal.* **28**, 119 (1986).
5. Savoretti, A. A., Borio, D. O., Bucala, V., and Porras, J. A., *Chem. Eng. Sci.* **54**, 205 (1999).
6. Chen, Q., Chen, X., Mao, L., and Cheng, W., *Catal. Today* **51**, 141 (1999).
7. Cavani, F., and Trifiro, F., *Appl. Catal.* **133**, 219 (1995).
8. Kolios, G., and Eigenberger, G., *Chem. Eng. Sci.* **54**, 2637 (1999).
9. Mimura, N., and Saito, M., *Catal. Today* **55**, 173 (2000).
10. Mimura, N., Takahara, I., Saito, M., Hattori, T., Ohkuma, K., and Ando, M., *Catal. Today* **45**, 61 (1998).
11. Addiego, W. P., Liu, W., and Boger, B., *Catal. Today* **69**, 25 (2001).
12. Miyakoshi, A., Ueno, A., and Ichikawa, M., *Appl. Catal., A: General* **216**, 137 (2001).
13. Meima, G. R., and Menon, P. G., *Appl. Catal., A: Gen.* **212**, 239 (2001).
14. Buyanov, R. A., Chesnokov, V. V., Afanas'ev, A. D., and Babenko, V. S., *Kinet. Catal.* **18**, 839 (1977).
15. Muhler, M., Schlögl, R., Reller, A., and Ertl, G., *Catal. Lett.* **2**, 203 (1989).
16. Muhler, M., Schlögl, R., Reller, A., and Ertl, G., *Appl. Catal.* **51**, 203 (1989).
17. Muhler, M., Schütze, J., Wesemann, M., Rayment, T., Dent, A., Schlögl, R., and Ertl, G., *J. Catal.* **126**, 339 (1990).
18. Muhler, M., Schlögl, R., and Ertl, G., *J. Catal.* **92**, 413 (1992).
19. Muhler, M., Schlögl, R., and Ertl, G., *J. Catal.* **138**, 413 (1992).
20. Joseph, Y., Ketteler, G., Kuhrs, C., Ranke, W., Weiss, W., and Schlögl, R., *Phys. Chem. Chem. Phys.* **3**, 4141 (2001).
21. Meima, G. R., and Menon, P. G., *Appl. Catal., A: Gen.* **212**, 239 (2001).

22. Lundin, J., Engvall, K., Holmlid, L., and Menon, P. G., *Catal. Lett.* **6**, 85 (1990).
23. Engvall, K., Holmlid, L., and Menon, P. G., *Appl. Catal.* **77**, 235 (1991).
24. Engvall, K., and Holmlid, L., *Appl. Surf. Sci.* **55**, 303 (1992).
25. Holmlid, L., Engvall, K., Aman, C., and Menon, P. G., *Stud. Surf. Sci. Catal.* **75**, 795 (1993).
26. Holmlid, L., and Menon, P. G., *Appl. Catal.* **212**, 247 (2001).
27. Engvall, K., Kotarba, A., and Holmlid, L., *Catal. Lett.* **26**, 101 (1994).
28. Engvall, K., Holmlid, L., Kotarba, A., Pettersson, J. B. C., Menon, P. G., and Skaugset, P., *Appl. Catal., A: Gen.* **134**, 239 (1996).
29. Kotarba, A., Engvall, K., Pettersson, J. B. C., Svanberg, M., and Holmlid, L., *Surf. Sci.* **342**, 327 (1995).
30. Engvall, K., Kotarba, A., and Holmlid, L., *J. Catal.* **181**, 256 (1999).
31. Barański, A., Dziembaj, R., Kotarba, A., Gołębiowski, A., Janecki, Z., and Pettersson, J. B. C., *Stud. Surf. Sci. Catal.* **126**, 229 (1999).
32. Kotarba, A., Dmytrzyk, J., Narkiewicz, U., and Barański, A., *React. Kinet. Catal. Lett.* **74**, 143 (2001).
33. Tomkowicz, Z., and Szytula, A., *J. Phys. Chem. Solids* **38**, 1117 (1977).
34. (a) Dudley, G. J., and Steele, B. C. H., *J. Solid State Chem.* **18**, 141 (1976); (b) Dudley, G. J., and Steele, B. C. H., *J. Solid State Chem.* **21**, 1 (1977).
35. Ito, S., Kurosawa, H., Akashi, K., Michiue, Y., and Watanabe, M., *Solid State Ionics* **86**, 745 (1996).
36. Ito, S., Washio, M., Makino, I., Koura, N., and Akashi, K., *Solid State Ionics* **86**, 1005 (1996).
37. Fan, L., Wen-Xiang, W., Qi-Kun, H., and Ling, W., *J. Solid State Chem.* **87**, 264 (1990).
38. Engvall, K., and Holmlid, L., *Appl. Surf. Sci.* **55**, 303 (1992).
39. Brundle, C. R., Chuang, T. J., and Wandelt, K., *Surf. Sci.* **68**, 459 (1977).
40. Wandelt, K., *Surf. Sci*. **1**, 2 (1982).
41. Sojka, Z, and Klier, K., *J. Electron. Spectrosc. Relat. Phenom.* **60**, 155 (1992).
42. De Angelis, B. A., *J. Electron. Spectrosc. Relat. Phenom.* **9**, 81 (1976).
43. Madey, T. E., Yakshinsky, B. V., Ageev, V. N., and Johnson, R. E., *J. Geophys. Res.* **103**, 5873 (1998).
44. Piskorz, W., *et al.*, *Phys. Chem. Chem. Phys.* in preparation.